# Hysteretic and chaotic dynamics of viscous drops in creeping flows with rotation

## Y.-N. YOUNG[1], J. BŁAWZDZIEWICZ[2], V. CRISTINI[3] AND R. H. GOODMAN[1]

[1]Department of Mathematical Sciences, New Jersey Institute of Technology, Newark, NJ 07102-1982, USA

[2]Department of Mechanical Engineering, Yale University, PO Box 20-8286, New Haven, CT, 06520-8286, USA

[3]School of Health Information Sciences and Biomedical Engineering, The University of Texas Health Science Center, Houston, TX 77030, USA

We have shown that high-viscosity drops in two-dimensional linear creeping flows with a non-zero vorticity component may have two stable stationary states. One state corresponds to a nearly spherical, compact drop stabilized primarily by rotation, and the other to an elongated drop stabilized primarily by capillary forces. Here we explore consequences of the drop bistability for the dynamics of highly viscous drops. Using both boundary-integral simulations and small-deformation theory we show that a quasi-static change of the flow vorticity gives rise to a hysteretic response of the drop shape, with rapid changes between the compact and elongated solutions at critical values of the vorticity. In flows with sinusoidal temporal variation of the vorticity we find chaotic drop dynamics in response to the periodic forcing. A cascade of period-doubling bifurcations is found to be directly responsible for the transition to chaos. In random flows we obtain a bimodal drop-length distribution. Some analogies with the dynamics of macromolecules and vesicles are pointed out.

## 1. Introduction

Investigations of dynamical properties of fluid–fluid dispersions, e.g. emulsions (Borwankar & Case 1997; Mason 1999) and polymer blends (Tucker III & Moldenaers 2002; Windhab *et al.* 2005), require detailed understanding of the behaviour of viscous drops in creeping flows. Such understanding is also crucial in the development of new drop-based microfluidic systems (Whitesides & Stroock 2001; Tan *et al.* 2004; Cristini & Tan 2004; Song, Chen & Ismagilov 2006; Grigoriev, Schatz, & Sharma 2006). Therefore, drop dynamics at small Reynolds numbers have been extensively studied experimentally (Torza, Cox & Mason 1972; Bentley & Leal 1986; Bigio, Marks & Calabrese 1998; Guido, Minale & Maffettone 2000; Cristini *et al.* 2003*b*; Guido, Grosso & Maffettone 2004) computationally (Rallison & Acrivos 1978; Kennedy, Pozrikidis & Skalak 1994; Cristini, BłAwzdziewicz & Loewenberg 1998; Zinchenko, Rother & Davis 1999; Cristini, BłAwzdziewicz & Loewenberg 2001; Cristini *et al.* 2003*b*; Renardy 2006) and theoretically (Barthès-Biesel & Acrivos 1973; Rallison 1980; Bławzdziewicz, Cristini & Loewenberg 2002, 2003; Vlahovska, BłAwzdziewicz & Loewenberg 2005).

These investigations revealed complex nonlinear drop dynamics resulting from the coupling between the drop shape and fluid flow. Examples of nonlinear phenomena

that occur under creeping-flow conditions include formation of self-similar neck regions during a drop breakup process (Bławzdziewicz, Cristini & Loewenberg 1997; Lister & Stone 1998), universal slow evolution of drops near the critical flow strength above which there are no stationary drop shapes (Bławzdziewicz, Cristini & Loewenberg 1998; Navot 1999; Bławzdziewicz *et al.* 2002), and existence of two branches of stable stationary shapes of highly viscous drops in two-dimensional Stokes flows with non-zero vorticity (Bławzdziewicz *et al.* 2003).

As revealed by the analysis presented by Bławzdziewicz *et al.* (2003), there exists a flow-parameter range where a high-viscosity drop can either adopt a nearly spherical shape stabilized primarily by the rotational flow component or an elongated shape stabilized primarily by capillary forces. Abrupt changes of the drop shape from one state to the other can be used in manipulation of emulsion microstructure and for controlling the behaviour of highly viscous drops in microfluidic devices. Due to discontinuous changes of emulsion microstructure, the bistable drop behaviour may also significantly affect emulsion rheology. The mechanism of the bistability is also of fundamental interest because of close analogies to the dynamics of vesicles (Misbah 2006; Mader *et al.* 2006; Vlahovska & Gracia 2007) and macromolecules (Bławzdziewicz 2006) in external flows.

Because of the fundamental significance and potential applications (such as those mentioned above), it is important to explore the dynamics of highly viscous drops in linear flows with non-zero vorticity. Our earlier investigation of this system (Bławzdziewicz *et al.* 2003) was limited to stationary drop shapes and stationary external flows. In the present study we thus focus on drop behaviour in time-dependent flows. We elucidate the physical mechanisms that gives rise to the bistable drop behaviour and examine the consequence of these mechanisms for drop response to time variation of the fluid vorticity.

The system dynamics is investigated via direct boundary-integral simulations (Pozrikidis 1992; Cristini *et al.* 2001; Bławzdziewicz 2006) and by using a small-deformation approach (Vlahovska 2003; Vlahovska *et al.* 2005). In particular, we show that the small-deformation equations with only several essential terms retained reproduce complex dynamical features of drop evolution that are associated with drop bistability.

To emphasize important aspects of the drop dynamics we consider three flow-variation protocols. In the first protocol, the vorticity is slowly increased and then decreased. We find that such quasi-static vorticity ramping gives access to both the elongated and compact, nearly spherical stationary drop shapes. The drop exhibits a hysteretic behaviour, with transitions between the compact shape (rotationally stabilized) and elongated shape (stabilized by capillary forces) occurring at different values of the vorticity when it is slowly ramped up or down.

In the second protocol, the vorticity undergoes finite-frequency harmonic oscillations. As expected, at low frequencies the drop behaviour is quasi-static, with a hysteresis loop analogous to the one observed for linear ramping. At high frequencies the vorticity variation averages out, and the drop undergoes small oscillations around the stationary shape corresponding to the average flow. However, at intermediate frequencies we find a much more complex behaviour. In particular we show that there exists a frequency and amplitude domain where the drop response to the periodic forcing is chaotic. Since in the creeping-flow regime fluid motion is governed by the linear Stokes equations, the nonlinear chaotic behaviour of the drop stems entirely from the coupling between the drop shape and the fluid flow. An analysis of drop motion in the chaotic domain indicates that the transition to

chaos is associated with the existence of two stationary states observed in steady flow.

In our third flow-variation protocol, the vorticity of the imposed flow undergoes random changes. We observe that the resulting statistical distribution of the drop length is bimodal in a certain regime of flow parameters, with two peaks around the drop length corresponding to the short and long stationary solutions. Hence, we find that, also in this problem, the existence of two stationary states underpins drop behaviour in time-dependent flow.

In §2 the system considered in our paper is defined. The quasi-static hysteretic drop behaviour is analysed in §3, our results for chaotic drop dynamics are presented in §4, and drop motion in linear flows with randomly varying vorticity is discussed in §5. Our findings are summarized in §6. In the Appendix we discuss some aspects of drop behaviour in a near-critical regime (i.e. close to a drop instability).

## 2. Viscous drops in two-dimensional linear flows

We consider a viscous drop suspended in an incompressible Newtonian fluid of a constant viscosity $\mu$. The viscosity of the drop fluid is $\hat{\mu} = \lambda\mu$, and the interfacial tension between the two phases is $\sigma$. The drop is surfactant-free, and no Marangoni stresses are present. There are also no buoyancy forces. We focus here on nonlinear effects that stem entirely from the coupling of the fluid flow to the drop shape (but not from the fluid inertia). Therefore, the creeping-flow conditions are assumed.

In the creeping-flow regime the fluid motion in the regions inside ($\mu_i = \hat{\mu}$) and outside ($\mu_i = \mu$) the drop is governed by the Stokes equations

$$\mu_i \nabla^2 \boldsymbol{u} = \nabla p, \tag{2.1}$$

$$\nabla \cdot \boldsymbol{u} = 0. \tag{2.2}$$

The fluid velocity $\boldsymbol{u}$ is continuous at the drop interface $\Omega$. Due to the absence of the Marangoni stresses the tangential viscous traction is also continuous. The jump in the normal viscous traction across $\Omega$ is equal to the capillary pressure

$$[\hat{\boldsymbol{n}} \cdot \boldsymbol{\tau} \cdot \hat{\boldsymbol{n}}] = 2\kappa\sigma, \tag{2.3}$$

where $\boldsymbol{\tau}$ is the viscous stress tensor, $\hat{\boldsymbol{n}}$ is the outward normal unit vector, and $\kappa$ is the local curvature.

The drop is subject to a two-dimensional linear incident flow

$$\boldsymbol{u}_0(\boldsymbol{r}) = \dot{\gamma}(\boldsymbol{E}_{\mathrm{s}} + \beta\boldsymbol{\Omega}) \cdot \boldsymbol{r}, \tag{2.4}$$

where $\dot{\gamma}$ is the strain rate, $\beta$ is the dimensionless vorticity parameter, $\boldsymbol{r}$ is the position, and $\boldsymbol{E}_{\mathrm{s}}$ and $\boldsymbol{\Omega}$ are the symmetric and antisymmetric parts of the normalized velocity-gradient tensor. In a conveniently chosen coordinate system we have

$$\boldsymbol{E}_{\mathrm{s}} = \frac{1}{2}\begin{pmatrix} 0 & 1 & 0 \\ 1 & 0 & 0 \\ 0 & 0 & 0 \end{pmatrix}, \qquad \boldsymbol{\Omega} = \frac{1}{2}\begin{pmatrix} 0 & 1 & 0 \\ -1 & 0 & 0 \\ 0 & 0 & 0 \end{pmatrix}, \tag{2.5}$$

without loss of generality. According to the above equations, $\beta = 0$ corresponds to a purely straining flow with the extensional axis $x = y$ and the compressional axis $x = -y$, and $\beta = 1$ corresponds to shear flow in the $x$ direction with the velocity gradient in the $y$ direction. The tensor $\boldsymbol{\Omega}$ in equation (2.4) describes the rigid-body
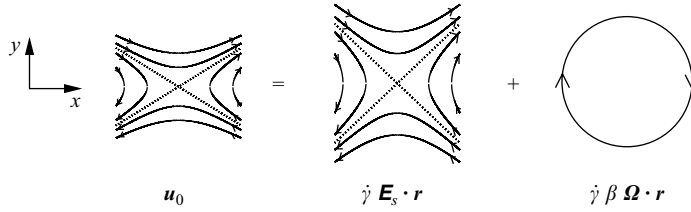
FIGURE 1. Decomposition of a linear incident flow into pure strain and rigid-body rotation.

rotation in the anticlockwise direction with the angular velocity

$$\omega = \tfrac{1}{2}\beta\dot{\gamma}. \tag{2.6}$$

The decomposition of the flow field (2.4) into the straining and rotational components (2.5) (as sketched in figure 1) is important for understanding of hysteretic and chaotic drop dynamics discussed in the following sections.

The dynamics of our system is characterized by three dimensionless parameters. There is the viscosity ratio $\lambda$ that characterizes dissipative forces in the drop- and continuous-phase fluids. The capillary number

$$Ca = \frac{a\mu\dot{\gamma}}{\sigma} \tag{2.7}$$

(where $a$ is the radius of an undeformed drop) characterizes the ratio between the deforming viscous forces produced by the imposed flow (2.4) and the capillary forces that resist drop deformation and drive the drop towards the equilibrium spherical shape. Finally, the vorticity parameter $\beta$ characterizes the magnitude of the rotational component of the external flow relative to the extensional component.

In this paper we focus on the parameter range where the drop deformation may be significant, which requires that $Ca = O(1)$. (However, the flow is not strong enough to cause drop breakup.) We also assume that the drop-phase fluid is much more viscous than the continuous-phase fluid,

$$\lambda \gg 1. \tag{2.8}$$

The drop-deformation process is hindered at large drop-phase viscosities, while drop rotation is only weakly affected by the viscous stresses inside the drops. Therefore, the relative effect of the drop rotation is amplified in the regime (2.8), and the rotational component of the external flow produces non-trivial qualitative effects.

## 3. Hysteretic drop behaviour
### 3.1. *Capillary and rotational stabilizing mechanisms*

To illustrate the effect of the rotational component of the flow (2.4) on the dynamics of a highly viscous drop, we consider a system where the parameter $\beta$ is first slowly increased and then slowly decreased. We adopt here a linear ramping protocol where the vorticity is slowly ramped up from $\beta = 0$ to $\beta = 0.4$ and then ramped down back to zero. Before the ramping occurs, the flow is maintained at $\beta = 0$ (for 5 % of the total ramping time) to allow the drop to relax to the stationary shape in purely straining flow. This vorticity variation protocol is represented in the inset of figure 2(*a*).

The evolution of the drop shape in this time-dependent flow is depicted in figure 2. Figure 2(*a*) represents the drop length *l*, and figure 2(*b*) shows the drop
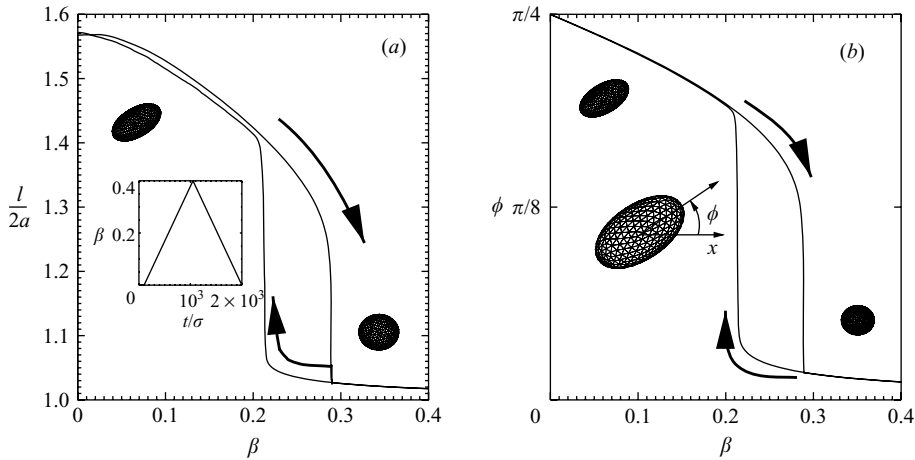
FIGURE 2. Hysteretic evolution of viscous drop in two-dimensional straining flow with slowly varying vorticity. Viscosity ratio $\lambda = 200$ and capillary number $Ca = 0.20$. (a) Normalized drop length $l$ and (b) drop angle $\phi$ (the angle between the drop major axis and the horizontal axis $x$, as shown in the inset) versus vorticity parameter $\beta$. Arrows indicate the direction of increasing time, and inset in panel (a) shows dependence of $\beta$ on time. (Results from boundary-integral simulations.)

angle $\phi$ (measured anticlockwise from the axis $x$, as defined in the inset); both quantities are plotted against the vorticity parameter $\beta$. In our example, the drop viscosity is $\lambda = 200$. The capillary number $Ca = 0.2$ is below the critical value for drop breakup ($Ca = 0.22$ in two-dimensional straining flow) but it is sufficiently large to allow for a significant flow-induced drop deformation. The total ramping time is $T = 2000 \lambda \mu a \sigma^{-1}$, so that the drop response to the flow variation is nearly quasi-static. The calculations were performed using the boundary-integral procedure developed by Cristini *et al.* (2001, 1998).

The results shown in figure 2 indicate that the drop response to the vorticity variation is hysteretic. At $\beta = 0$ the drop is elongated, and it is aligned with the extensional axis of the straining component of the flow ($\phi = \pi/4$). With increasing $\beta$, the drop orientation slowly changes towards the symmetry axis $x$ ($\phi = 0$), and the drop length slowly decreases. At a critical value of the vorticity parameter, $\beta_2 \approx 0.29$, a discontinuous change occurs: the drop length and the angle suddenly decrease. Afterwards the drop is almost spherical and nearly aligned with the axis $x$. When the direction of the vorticity change is reversed, the drop initially retraces its trajectory. However, the drop does not jump back to the elongated shape until the vorticity reaches the lower critical value $\beta_1 \approx 0.22 < \beta_2$.

The bistable drop behaviour and the associated hysteretic shape evolution stem from the existence of two mechanisms that can stabilize a viscous drop in linear flows with rotation (2.4). Namely, the drop can be stabilized by the capillary stresses (which drive the drop towards the equilibrium spherical shape) or by the vorticity flow component (which rotates the drop out of the extensional axis of the straining component of the flow).

In a purely straining flow the drop assumes the interfacial-tension-stabilized elongated shape (Taylor 1934). The stationary drop shape results from the balance between drop deformation by the flow and drop relaxation due to the capillary forces.
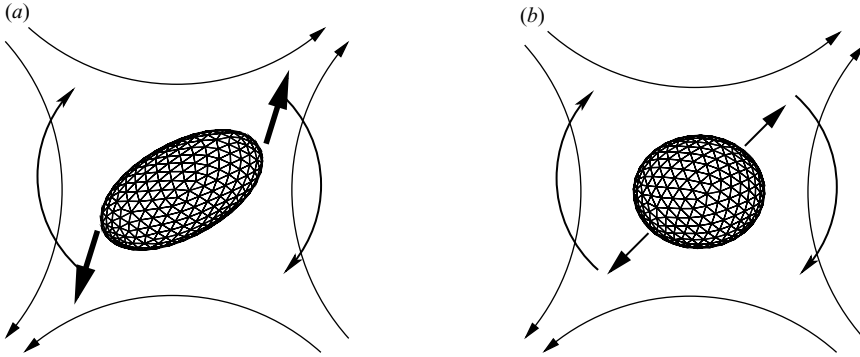
FIGURE 3. Schematic representation of the physical mechanism leading to bistable drop behaviour in two-dimensional linear flows with non-zero vorticity. (*a*) The elongated drop is stabilized by capillary forces and destabilized by flow rotation; (*b*) the compact drop is stabilized by flow rotation and destabilized by extensional flow component.

The deformation and relaxation occur on the respective time scales

$$t_\gamma = \lambda \dot{\gamma}^{-1}, \tag{3.1}$$

$$t_\sigma = \lambda \mu a \sigma^{-1}, \tag{3.2}$$

both of which are proportional to the viscosity ratio for $\lambda \gg 1$. The drop deformation $D = (l - 2a)/a$ is determined by the time scale ratio

$$D \sim t_\sigma / t_\gamma = Ca, \tag{3.3}$$

and therefore it is independent of the viscosity ratio in the limit $\lambda \to \infty$. In purely straining flows, the drop is oriented along the extensional axis $x = y$.

For small values of $\beta$, the vorticity flow component produces an $O(\beta)$ perturbation of the drop orientation. The corresponding decrease of the drop length is $O(\beta^2)$. However, a further rotational motion of the drop is arrested because the straining component of the flow produces hydrodynamic stresses that pull the elongated drop back towards the straining axis (as illustrated in figure 3a).

Since the $O(\lambda^{-1})$ internal circulation inside an elongated high-viscosity drop is weak, the drop in its stationary state behaves analogously to a rigid body whose equilibrium orientation results from the balance of the torques produced by the straining and rotational components of the external flow. The transition to the compact drop shape occurs when the vorticity flow component becomes too strong to be balanced. Under such conditions, a rigid body would undergo a transition to a periodic motion with continuous rotation in the clockwise direction. For similar reasons, a drop also starts to rotate continuously when $\beta$ achieves the upper critical value $\beta_2$. During the rotation the drop length decreases because the drop becomes misaligned with the extensional axis of the flow. As a result, the drop relaxes to a nearly spherical shape.

In this new, compact shape the fluid inside the drop circulates with the angular velocity $\omega_d$ that is nearly equal to the angular velocity of the external flow (2.6). Within each period of rotation the drop undergoes a small deformation produced by the straining component of the external flow (as schematically illustrated in figure 3b). However, the deformation does not accumulate because it is constantly convected away by the rotational component of the flow. Since the rotation occurs on the time scale

$$t_{rot} = (\beta \dot{\gamma})^{-1}, \tag{3.4}$$

and the drop deforms on the much longer time scale (3.1), we find that the drop deformation in the compact state,

$$D \sim t_{rot}/t_\gamma = (\beta\lambda)^{-1}, \tag{3.5}$$

is small for $\lambda \gg 1$, consistent with the results shown in figure 2($a$).

Relation (3.5) indicates that the deformation of the rotationally stabilized drop increases with the decreasing parameter $\beta$. When $\beta$ falls below the lower critical value $\beta_1$, the hydrodynamic torque associated with the straining component of the flow acting on a slightly elongated drop becomes strong enough to reorient the drop towards the straining axis and arrest further drop rotation. Deformation thus starts to accumulate, the drop is stretched, and a transition to the interfacial-tension-stabilized elongated state takes place.

As shown in figure 2, a drop in the compact, rotationally stabilized stationary state is nearly aligned with the symmetry axis of the applied flow $x$. This behaviour stems from the flow-reflection symmetry of Stokes equations and the fact that the drop is stabilized by rotation rather than the capillary forces. In the absence of the capillary forces (or in the limit of infinitely strong flow) the symmetry of Stokes equations implies that the stationary drop shape is invariant with respect to the flow reflection. Hence, the shape is also invariant with respect to the corresponding transformation $(x, y, z) \rightarrow (-x, y, z)$ of the spatial coordinates (i.e. the reflection of the drop shape in the $y$–$z$ plane), and this symmetry corresponds to drop alignment in the $x$ direction. A perturbation due to the presence of the capillary stresses produces only a small asymmetry because the effect of capillary forces is insignificant for a nearly spherical drop.

### 3.2. *Parameter dependence of drop response*

#### 3.2.1. *Simulation results*

The quasi-static response of the drop length to the variation of the vorticity is illustrated in figure 4 for different values of the capillary number $Ca$ and viscosity ratio $\lambda$. The corresponding drop angle is shown in figure 5. The results indicate that the size of the hysteresis loop (in both drop length and angle) is the largest for large values of $\lambda$ and $Ca$. When the capillary number is decreased, the upper critical vorticity parameter $\beta_2$ (corresponding to the transition from the elongated to the compact drop) decreases but the lower critical parameter $\beta_1$ remains nearly unaffected. In contrast, the viscosity ratio $\lambda$ affects primarily the position of the lower critical parameter $\beta_1$ (corresponding to the transition from the compact to the elongated drop).

This behaviour is consistent with the scaling relations (3.3) and (3.5) and the mechanism of drop bistability explained in §3.1. According to our analysis, the critical states associated with the transitions between the elongated and compact drop shapes correspond to the parameter values where the maximal torque $\tau_\gamma$ exerted by the extensional component of the flow on the drop marginally balances the torque $\tau_{rot}$ exerted by the vorticity flow component. Since the straining component of the flow produces a non-zero torque only on elongated shapes, and $\tau_{rot}$ is approximately independent of $D$, we obtain the scaling relations

$$\tau_\gamma \sim D, \qquad \tau_{rot} \sim \beta. \tag{3.6}$$

Assuming the torque balance
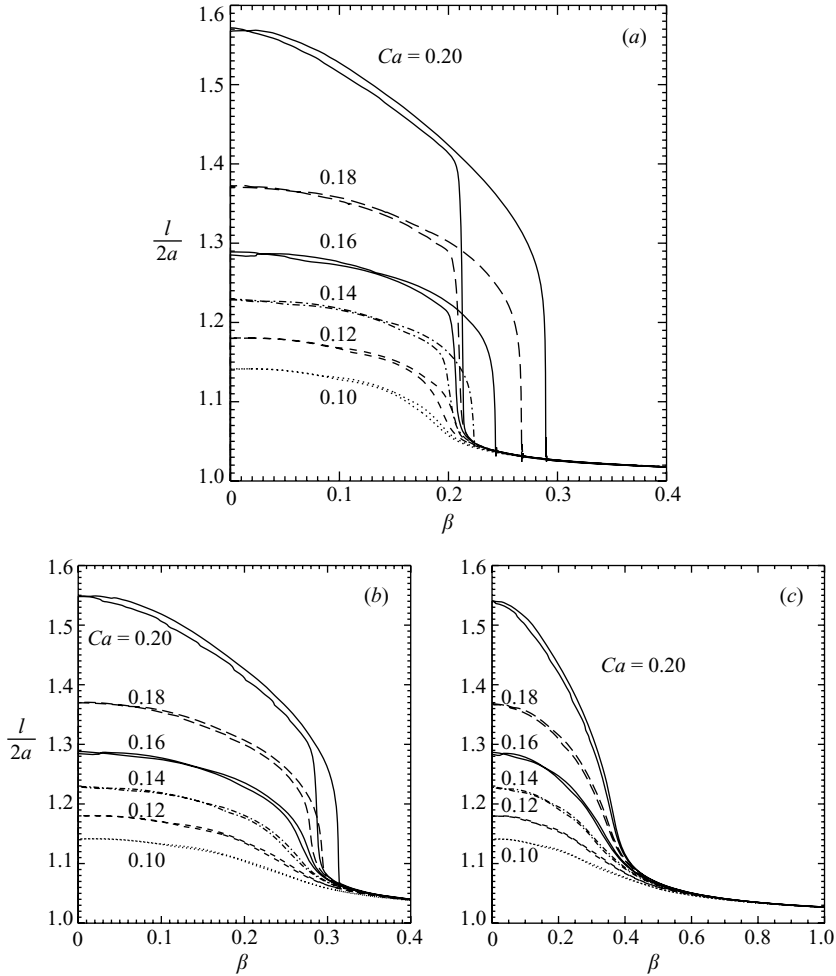
$$\tau_\gamma \approx \tau_{rot}, \tag{3.7}$$

FIGURE 4. Quasi-static variation of drop length $l$ with vorticity parameter $\beta$ for (a) $\lambda = 200$, (b) 100, (c) 50, and different values of capillary number (as labelled). (Results from boundary-integral simulations.)

near a transition point and combining relations (3.6) with the estimates (3.5) and (3.3) for the drop deformation in the compact and elongated states, we find the scaling relations

$$\beta_1 \sim \lambda^{-1/2}, \tag{3.8}$$

$$\beta_2 \sim Ca \tag{3.9}$$

for the lower and upper critical vorticity parameters.

Both scaling relations (3.8) and (3.9) are consistent with our simulation results shown in figure 4. Relation (3.8) also agrees with the asymptotic result result (3.22), which is obtained in §3.3 using a small-deformation theory.

The plots shown in figure 4 indicate that for a given viscosity ratio, there exists a critical value of the capillary number $Ca^\star$ below which the drop response to the changes of the flow vorticity does not exhibit a hysteretic loop. The bifurcation point occurs at the critical value of the vorticity parameter $\beta^\star$ that corresponds to
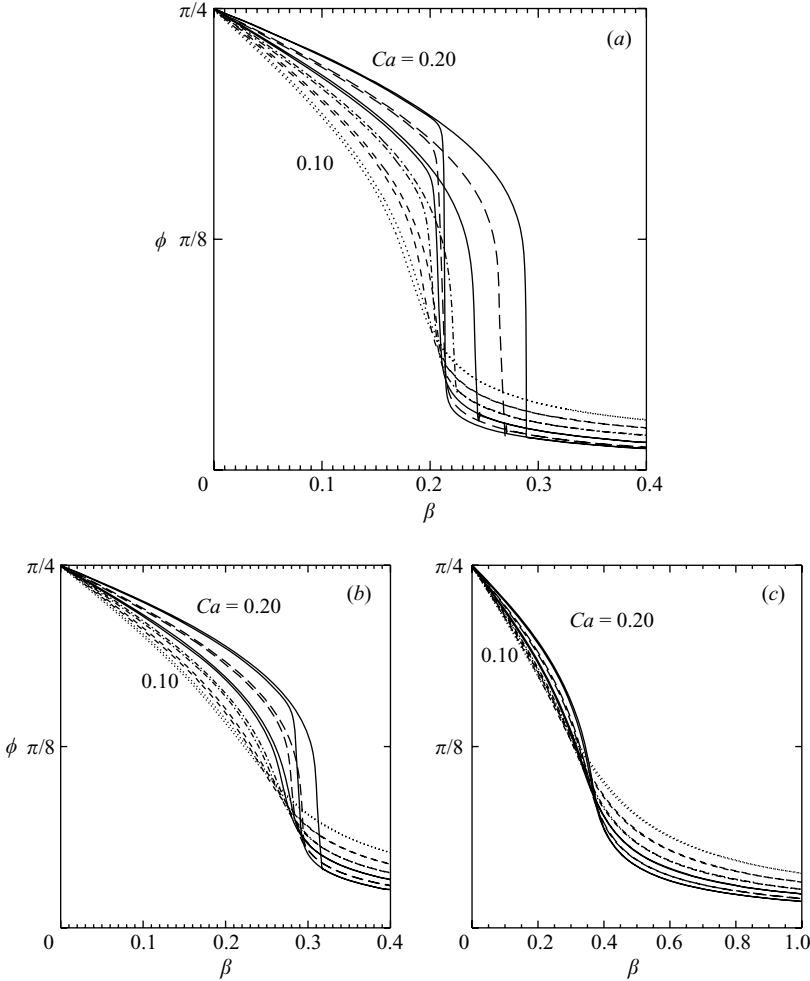
FIGURE 5. Quasi-static variation of drop angle $\phi$ with vorticity parameter $\beta$ for (a) $\lambda = 200$, (b) 100 and (c) 50. Different curves correspond to different values of capillary number as labelled in figure 4.

the position of the infinitesimal hysteresis loop for $Ca$ slightly above the critical value $Ca^\star$. Noting that the hysteresis loop disappears when $\beta_1 = \beta_2$, we find from the estimates (3.8) and (3.9) that $Ca^\star \sim \lambda^{1/2}$ and $\beta^\star \sim \lambda^{1/2}$. These scaling relations agree with the earlier asymptotic analysis by Bławzdziewicz *et al.* (2003), who have shown that the cusp bifurcation resulting in the hysteretic drop behaviour occurs at

$$Ca^\star = \frac{16}{19} \left( \frac{5}{\lambda} \right)^{1/2}, \qquad \beta^\star = \frac{3}{4} \left( \frac{15}{\lambda} \right)^{1/2}, \qquad (3.10)$$

where $\lambda \gg 1$ is assumed. (See equations (16) in Bławzdziewicz *et al.* 2003, and note the difference in the definition of capillary number.)

Relations (3.10) indicate that the transition between the hysteretic and non-hysteretic behaviour occurs at $Ca^\star \approx 0.13$ for $\lambda = 200$ and $Ca^\star \approx 0.19$ for $\lambda = 100$; the corresponding positions of the infinitesimal hysteresis loops are $\beta^\star \approx 0.21$ and $\beta^\star \approx 0.29$. The above estimates are consistent with the results shown in figures 4(a)

and 4(b). For $\lambda = 50$, equation (3.10) predicts $Ca^\star \approx 0.26$, which is above the critical capillary number for drop breakup, $Ca_{crit} = 0.22$. Hence, the elongated stationary drop shape does not exist for $Ca > Ca^\star$, and therefore there is no hysteretic loop seen in figure 4(c).

### 3.2.2. *Numerical accuracy*

Numerical simulations presented in this paper were performed using the adaptive boundary-integral procedure developed by Cristini *et al.* (1998, 2001). The maximal number of nodes on the drop surface during the simulation runs shown in figures 2, 4, and 5 ranged from $N = 362$ for $Ca = 0.1$ and $\lambda = 50$ to $N \approx 10^3$ for $Ca = 0.2$ and $\lambda = 200$. The time-stepping was performed using the second-order Runge–Kutta method. The total ramping time ranged from $T = 250 t_\sigma$ for small values capillary number and viscosity to $T = 2000 t_\sigma$ for the most difficult simulation of the system with $Ca = 0.2$ and $\lambda = 200$. Numerical accuracy of the results is within 2 %.

Simulations of hysteretic drop evolution are numerically demanding, owing to high drop viscosity and close proximity to bifurcation points corresponding to the transitions between the elongated and compact stationary drop shapes. For $Ca = 0.2$ and moderate values of $\beta$ the system is also close to the critical point for drop breakup, which adds to a further increase of the numerical cost. As explained in the Appendix, in the neighbourhood of critical points drop evolution exhibits (a) critical slowing down and (b) large susceptibility to small perturbations of the system parameters. We find that the critical slowing down is responsible for somewhat blurred transition between the hysteretic and non-hysteretic drop behaviour seen in figures 4(a), 4(b), 5(a) and 5(b). The large susceptiblity of the system to small perturbations associated with the discretization errors is the main cause of the approximately 1 % difference in the drop length as the vorticity is slowly ramped up and then down along the branch of elongated solutions ($\beta < \beta_1$). The corresponding inaccuracy of the drop angle is smaller.

### 3.3. *Small-deformation analysis*

#### 3.3.1. *Evolution equations*

Crucial features of the evolution of a highly viscous drop in two-dimensional flows with non-zero vorticity are well captured by small-deformation equations. In our approach (Bławzdziewicz *et al.* 2003; Vlahovska 2003; Vlahovska *et al.* 2005), the position $r_S$ of the drop interface is expanded in spherical harmonics,

$$r_S/a = \alpha' + \sqrt{2} \sum_{l,m} [f'_{lm} \mathrm{Re}(Y_{lm}) + f''_{lm} \mathrm{Im}(Y_{lm})], \qquad (3.11)$$

where $l > 0$ and $l \geqslant m \geqslant 0$ denote the spherical-harmonic order, $f'_{lm}$ and $f''_{lm}$ are the expansion coefficients, and the parameter $\alpha'$ is given by the drop-volume constraint. Since for $m = 0$ all spherical harmonics are real, we set $f''_{l0} = 0$ in expansion (3.11). Moreover, flow-induced drop deformation preserves the symmetry of the incident flow (2.4). Therefore only even values of $l$ and $m$ need to be included in the analysis.

Evolution equations for the expansion coefficients $f'_{lm}$ and $f''_{lm}$ are obtained by inserting the series (3.11) into the boundary-value problem (2.1)–(2.5), performing a boundary-perturbation analysis, and re-expanding resulting products of spherical harmonics using appropriate Clebsch–Gordan coupling coefficients. The detailed analysis and explicit expressions for the evolution equations at different truncation levels are presented elsewhere (Vlahovska 2003; Vlahovska *et al.* 2005; Vlahovska, Bławzdziewicz & Loewenberg 2008).

For simplicity, our small-deformation calculations are performed with the expansion (3.11) truncated at the lowest spherical-harmonic order $l = 2$, which leaves us with three independent drop shape components: $f'_{22}$, $f''_{22}$, and $f'_{20}$. Noting that

$$\mathrm{Re}(Y_{22}) \sim \cos 2\phi, \qquad \mathrm{Im}(Y_{22}) \sim \sin 2\phi, \tag{3.12}$$

we find that the shape parameters $f'_{22}$ and $f''_{22}$ correspond to the drop deformation along the symmetry axis $x$ and the straining axis $x = y$, respectively. The parameter $f'_{20}$ describes an axisymmetric deformation along the axis $z$.

The evolution equations for the shape parameters $f'_{22}$, $f''_{22}$, and $f'_{20}$, truncated at the second-order in the drop deformation, can be represented in the following form,

$$\dot{f}'_{20} = \lambda^{-1}(d_{11} + d_{12}f'_{20})f''_{22} - \lambda^{-1}Ca^{-1}\left[D_1 f'_{20} - D_2\left(f'^2_{20} - f'^2_{22} - f''^2_{22}\right)\right], \tag{3.13a}$$

$$\dot{f}'_{22} = -2\omega f''_{22} + \lambda^{-1}\left[d_{21}f'_{22}f''_{22} - Ca^{-1}(D_1 + 2D_2 f'_{20})f'_{22}\right], \tag{3.13b}$$

$$\dot{f}''_{22} = 2\omega f'_{22} + \lambda^{-1}\left[(d_{31} + d_{32}f'_{20} + d_{33}f'^2_{20} + d_{34}f'^2_{22} + d_{35}f''^2_{22}) - Ca^{-1}(D_1 + 2D_2 f'_{20})f''_{22}\right], \tag{3.13c}$$

where the dot denotes the time derivative (normalized by $\dot{\gamma}^{-1}$). The terms involving the coefficients $d_{ij}$ correspond to drop deformation by the external flow, and the terms involving $D_k$ describe the capillary relaxation. All these terms are $O(\lambda^{-1})$ in the large-viscosity-ratio regime. Explicit expressions for the coefficients $d_{ij}$ and $D_k$ are given in (Vlahovska 2003; Vlahovska *et al.* 2008); here we only note that these coefficients are functions of the viscosity ratio $\lambda$ and have finite limits for $\lambda \to \infty$.

The two remaining terms on the right-hand side of equations (3.13b) and (3.13c) (i.e. the terms proportional to $\omega$) are viscosity-independent. These terms represent the rigid-body rotation of the drop, with the angular velocity

$$\omega = -\tfrac{1}{2}\beta + \tfrac{1}{2}c_1 f'_{22}, \tag{3.14}$$

where $c_1 = (15/2\pi)^{1/2}$. Consistent with our qualitative physical picture described in §3.1 (and illustrated in figure 3), the rotational velocity (3.14) involves two terms. The first term corresponds to the rotation of the drop by the vorticity component of the flow (2.4). The second term, which is proportional to the shape parameter $f'_{22}$ that described deformation in the $x$ direction, corresponds to the rotation of a deformed drop by the straining component of the external flow towards the straining axis $x = y$.

### 3.3.2. *Reduced description*

It has been shown by Błasdziewicz *et al.* (2003) that for $\lambda \gg 1$ the drop behaviour near the bifurcation point (3.10) can be described by simplified asymptotic equations

$$\dot{f}'_{22} = -2\omega f''_{22} - \lambda^{-1}Ca^{-1}\bar{D}_1 f'_{22}, \tag{3.15a}$$

$$\dot{f}''_{22} = 2\omega f'_{22} - \lambda^{-1}Ca^{-1}\bar{D}_1 f''_{22} + \lambda^{-1}\bar{d}_{31}. \tag{3.15b}$$

where $\bar{D}_1 = 20/19$ and $\bar{d}_{31} = (5\pi/6)^{1/2}$ are the high-viscosity limits of $D_1$ and $d_{31}$. The asymptotic result (3.15) is obtained from (3.13) on assumption that near the bifurcation point there is a balance between drop deformation and rotation (which corresponds to $\lambda^{-1} \sim \omega f'_{22}$) and the balance between capillary relaxation and rotation (which yields $(\lambda Ca)^{-1}f'_{22} \sim \omega f''_{22}$ and $(\lambda Ca)^{-1}f''_{22} \sim \omega f'_{22}$). Moreover, it is assumed that the two contributions to the angular velocity (3.14) are of the same order but do not cancel (i.e. $\omega \sim \beta \sim f'_{22}$). Equations (3.13) are rescaled accordingly, and only the leading-order terms are retained.

Equations (3.15) have all necessary ingredients that are needed to describe the hysteretic drop behaviour. There are terms representing drop rotation by the straining and vorticity components of the external flow (i.e the terms proportional to $\omega$), drop relaxation due to the presence of the capillary forces (the terms proportional to $Ca^{-1}$), and stretching of the drop along the extensional axis $x = y$ (the last term in equation (3.15b)). Neglecting any of these terms would qualitatively alter the solution structure, which would no longer manifest the key features of the drop evolution in the parameter range considered herein.

We expect the simplified small-deformation equation (3.15) to yield not only a qualitative but also a quantitative description of the bistable drop behaviour for a large portion of the hysteresis loops depicted in figures 2, 4, and 5. Significant deviations are expected only for the elongated states outside the small-capillary-number regime, especially for small values of the vorticity parameter $\beta$.

The range of validity of the small-deformation description can be extended to the domain of moderately large capillary numbers by using complete second-order equations (3.13). (One can also include higher-order spherical harmonics and higher-order terms in the expansion of the evolution equations in the shape parameters; these higher order-contributions were derived by Vlahovska 2003; Vlahovska *et al.* 2005; Vlahovska *et al.* 2008). The accuracy of the small-deformation equations is further discussed in § 3.3.4.

### 3.3.3. *Asymptotic solution*

In the regime $\lambda^{-1} \ll 1$ and $\beta \ll 1$ the stationary solutions of equations (3.15) can be obtained by a singular-perturbation analysis. To leading order in the small parameters, we find that the elongated drop is described by the relations

$$\omega \simeq 0, \qquad (3.16a)$$

$$\lambda^{-1} Ca^{-1} \bar{D}_1 f_{22}'' \simeq \lambda^{-1} \bar{d}_{31}. \qquad (3.16b)$$

The first of the above expressions corresponds to the fact that an elongated drop does not rotate (there is only a weak fluid circulation inside it, as predicted by our qualitative analysis). The second relation describes the balance between drop deformation by the external flow and relaxation due to the capillary forces. Recalling the definition (3.14) of the angular velocity $\omega$, we find that (3.16) yields

$$f_{22}' \simeq c_1 \beta, \qquad (3.17a)$$

$$f_{22}'' \simeq \bar{D}_1^{-1} \bar{d}_{31} \, Ca. \qquad (3.17b)$$

By inserting the above relations back into (3.15) one can verify that they constitute a leading-order asymptotic stationary solution.

According to equation (3.17b), drop elongation along the straining axis $x = y$ (i.e. $\phi = \pi/4$) scales with the capillary number, which is consistent with the estimate (3.3). The drop angle

$$\phi = \tfrac{1}{2} \arctan(f_{22}''/f_{22}') \qquad (3.18)$$

only slightly deviates from $\phi = \pi/4$ because $f_{22}' \ll f_{22}''$ (assuming that $Ca \gg \beta$ and $\beta \ll 1$).

The leading-order stationary solution corresponding to the compact drop is obtained from the relations

$$-2\omega f_{22}'' \simeq 0, \qquad (3.19a)$$

$$2\omega f_{22}' \simeq -\lambda^{-1} \bar{d}_{31}, \qquad (3.19b)$$

which are obtained by dropping from the evolution equations (3.15) the $O(\lambda^{-1})$ capillary-relaxation terms. Taking into account the definition (3.14) of $\omega$ we thus obtain

$$f''_{22} \simeq 0 \qquad (3.20a)$$

and

$$f'_{22} \simeq \frac{\beta - \sqrt{\beta^2 - 4c_1 \bar{d}_{31}\lambda^{-1}}}{2c_1} \qquad (3.20b)$$

(the solution with the plus sign in front of the square root is unstable).

Since the shape parameter $f''_{22}$ vanishes according to equation (3.20a), the drop is oriented in the $x$ direction. For $\lambda^{-1} \ll \beta^2$ we find

$$f'_{22} = \bar{d}_{31}(\beta\lambda)^{-1}, \qquad (3.21)$$

which is consistent with our scaling estimate (3.5). In the regime $\beta < \beta_1$, where

$$\beta_1 = 2(c_1\bar{d}_{31})^{1/2}\lambda^{-1/2}, \qquad (3.22)$$

the solution (3.20b) does not exist; the drop thus undergoes a transition to the elongated shape when $\beta$ drops below the critical value $\beta_1$. Inserting numerical values of the parameters $c_1$ and $\bar{d}_{31}$ into (3.22), we find $\beta_1 = (10/\lambda)^{1/2}$, in quantitative agreement with our numerical results presented in figure 4.

The solutions and (3.17) and (3.20) of the simplified small-deformation equations (3.15) are perturbative. However, the exact stationary solution can also be found (Bławzdziewicz *et al.* 2003). As shown in the following sections, our analytical solutions quantitatively agree with the results of numerical simulations, provided that the drop deformation is not too large.

### 3.3.4. *Numerical results*

Predictions of the small-deformation equations (3.13) for drop behaviour in two-dimensional linear flows with slowly varying vorticity are depicted in figure 6 for a system with viscosity ratio $\lambda = 200$. Figures 6(*a*) and 6(*b*) show the dependence of the drop length evaluated to leading order in the shape parameter,

$$\frac{l}{2a} = 1 + \sqrt{\frac{15}{8\pi}} \left(f'^2_{22} + f''^2_{22}\right)^{1/2}, \qquad (3.23)$$

and angle (3.18) on the vorticity parameter $\beta$ for the same set of capillary numbers as those represented in figures 4 and 5. In figures 6(*c*) and 6(*d*), the small-deformation results are compared directly with the results of the boundary-integral simulations. The small-deformation calculations were performed using the second-order equations (3.13) because for an elongated drop they are more accurate than the simplified equations (3.16).

The results shown in figure 6 indicate that for small and moderate capillary numbers the small-deformation theory yields accurate quantitative predictions. At higher values of $Ca$ drop behaviour is also captured quantitatively, except for the upper portion of the hysteresis loop (i.e. when the drop is in the elongated state). For all values of the capillary number, the lower and upper critical vorticity parameters $\beta_1$ and $\beta_2$ are obtained within the numerical error of the boundary-integral simulations. Our additional calculations (not shown) indicate that a similar accuracy is obtained for $\lambda = 50$ and $\lambda = 100$. The range of capillary numbers for which the deformation of the drop in elongated stationary state is reproduced accurately is consistent with
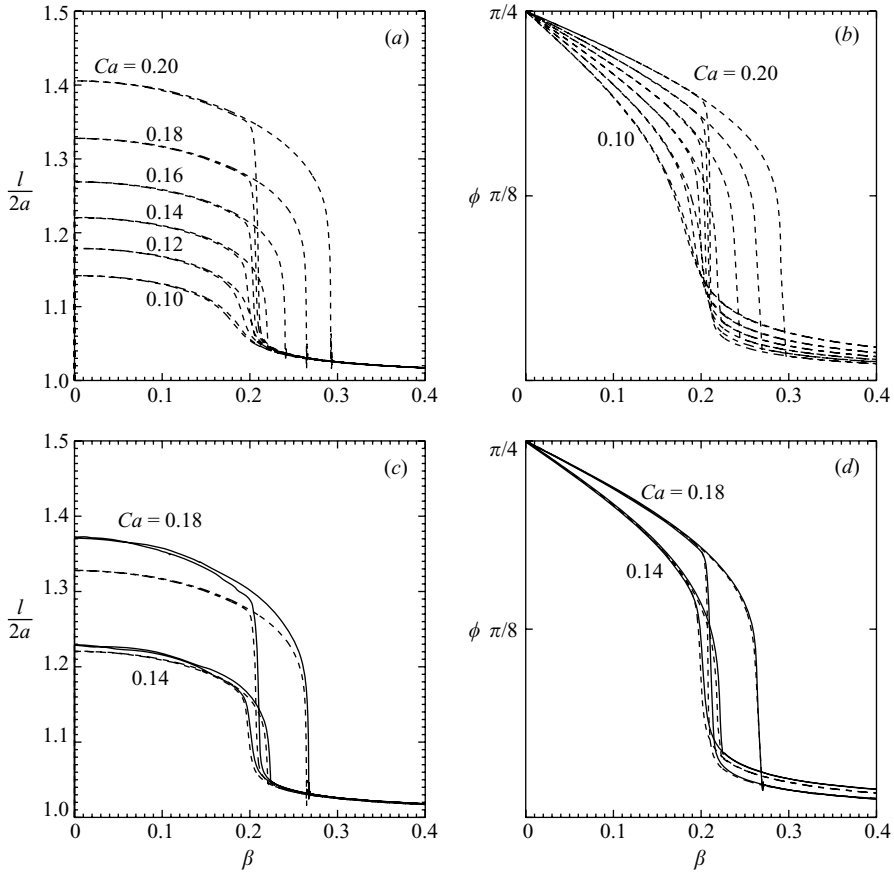
FIGURE 6. Quasi-static variation of drop length $l$ and angle $\phi$ with vorticity parameter $\beta$ for $\lambda = 200$ and different values of capillary number (as labelled). (*a, b*) Solution of small-deformation equations (3.13); (*c, d*) comparison of small-deformation results (dashed lines) with boundary-integral simulations (solid lines).

previously reported results for moderate drop viscosities (Vlahovska 2003; Vlahovska *et al.* 2005).

## 4. Chaotic drop dynamics in a sinusoidal straining flow

Dynamical systems with multiple equilibrium states often exhibit novel dynamics when driven by simple forcing (Guckenheimer & Holmes 1983*b*). Thus, despite the laminar nature of the Stokes flow, we expect to find interesting nonlinear dynamics of a viscous drop in a time-varying linear flow with rotation. To explore this dynamics we will now investigate the drop response to harmonic variation of the vorticity

$$\beta(t) = \bar{\beta} + \delta\beta \cos(2\pi t/T), \tag{4.1}$$

where $\bar{\beta}$ is the average vorticity value, $\delta\beta$ is the oscillation amplitude, and $T$ is the oscillation period.

We have performed a series of small-deformation calculations (§4.1) and boundary-integral simulations (§4.2) for different values of the flow parameters $\bar{\beta}$, $\delta\beta$, and $T$. If the oscillation period $T$ is much shorter than the drop–deformation and
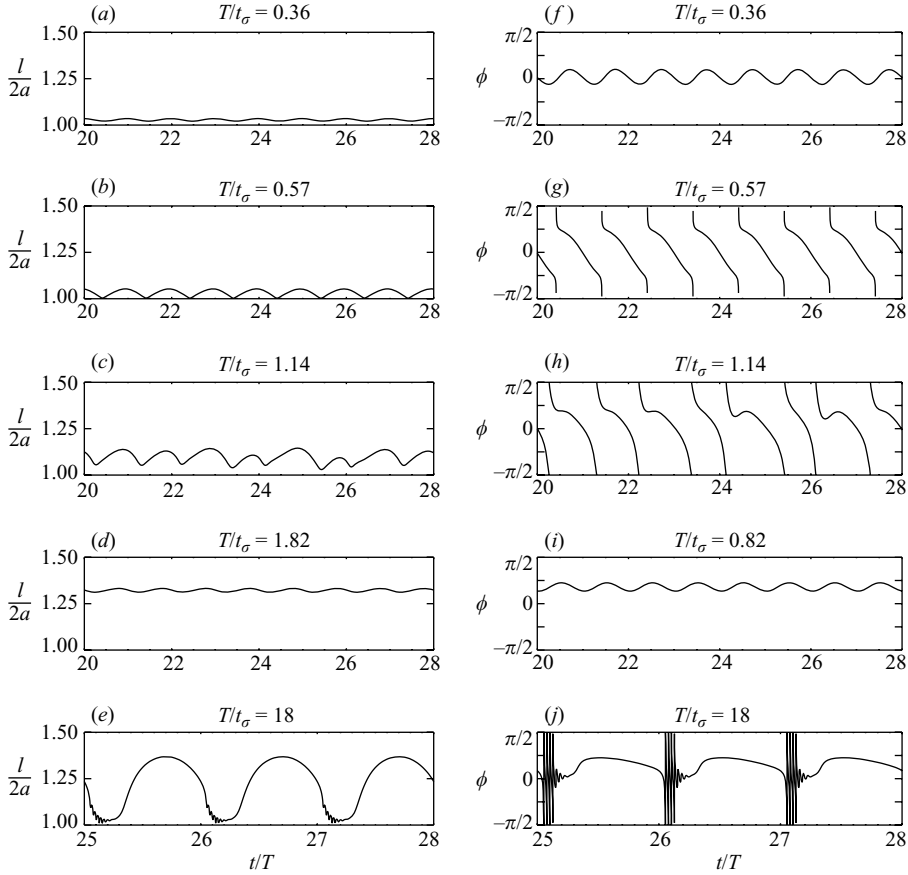
FIGURE 7. Evolution of drop length (*a–e*) and angle (*f–j*) in two-dimensional linear flow with harmonic variation of vorticity (4.1), for different values of period $T$ normalized by drop-relaxation time (as labelled). Mean vorticity $\bar{\beta} = 0.21$, vorticity amplitude $\delta\beta = 0.13$, viscosity ratio $\lambda = 275$, and capillary number $Ca = 0.2$. (*c, h*) Chaotic dynamics. (Results from small-deformation theory.)

drop-relaxation times (3.1) and (3.2), we find that the drop undergoes small oscillations about a stationary shape corresponding to the mean value of $\beta$ (which is an expected behaviour). In the opposite regime $T \gg t_\gamma, t_\sigma$, the quasi-static drop behaviour described in §3 is recovered. In what follows we focus on the most interesting parameter domain $T \sim t_\gamma, t_\sigma$ and $\delta\beta \sim \beta_1 - \beta_2$, in which an interaction of different timescales as well as an interplay between the short and elongated drop shapes is anticipated.

### 4.1. *Small-deformation results*

Figure 7 illustrates the dependence of the drop evolution in linear flow with the oscillatory vorticity (4.1) on the oscillation period $T$. The viscosity ratio in this example is $\lambda = 275$, and the capillary number is $Ca = 0.2$. The mean value of the vorticity $\bar{\beta} = 0.21$ is close to the lower critical value $\beta_1 = 0.19$, and the oscillation amplitude is $\delta\beta = 0.13$. Figure 7(*a–e*) shows the evolution of the drop length, and figure 7 (*f–j*) depicts the evolution of drop angle with respect to the axis $x$. Since the drop shape

is point-symmetric, we restrict the angle $\phi$ to the domain $(-\pi/2, \pi/2)$ by identifying drop configurations that differ by $\pi$.

Figure 7($a$, $f$) represents our results for the shortest oscillation period of the flow vorticity $T/t_\sigma = 0.36$. The drop oscillates about the compact stationary shape in this case. Both the drop length and angle vary periodically, with the period $T_d$ equal to the period $T$ of the external forcing. The drop length decreases when the drop is in the compressional quadrant $-\pi/2 < \phi < 0$ and increases for $0 < \phi < \pi/2$. We find that upon an increase of the period of the external forcing the amplitude of the angular drop oscillations increases. When the oscillation amplitude reaches $\pi/2$ the drop starts to tumble, which corresponds to $d\phi/dt < 0$ over the whole period of motion, as illustrated in figure 7($b$, $g$). (Note that the angles $\phi = -\pi/2$ and $\pi/2$ describe the same drop configuration, so there are no discontinuities in the drop evolution.)

A further increase of the period of the external forcing results in a qualitative change of drop response. We find that the drop still undergoes a tumbling motion; however, the evolution is not periodic but it becomes *chaotic*, as shown in figure 7($c$, $h$). The chaotic motion continues up to $T/t_\sigma = 1.37$, and then the drop reverts to periodic motion. For $T/t_\sigma = 1.82$ (figure 7$d$, $i$) the drop oscillates about the elongated stationary shape, and in the regime $T/t_\sigma \gg 1$ (figure 7$e$, $j$) the system approaches the quasi-static behaviour discussed in §3.†

The transition to the chaotic drop motion occurs through a cascade of period-doubling events, as illustrated in figures 8 and 9. Figure 8 depicts the drop evolution at two values of the amplitude of vorticity oscillations $\delta\beta$ (the remaining system parameters are the same as those that yield the chaotic motion depicted in figure 7$c$, $h$). The results shown in figure 8($a$) indicate that for a sufficiently small oscillation amplitude ($\delta\beta = 0.06$ in our example) the drop evolves with the period $T_d = T$ (i.e. the period equal to that of the external forcing). At a larger amplitude $\delta\beta = 0.08$ the drop oscillation period is $T_d = 2T$ (cf. figure 8$b$) and for $\delta\beta = 0.083$ we find $T_d = 4T$ (not shown). The period-doubling scenario of the transition to chaos in our system is further supported by the bifurcation diagrams depicted in figure 9, where the drop length $l$ at times $t = nT$ ($n = 1, 2, \ldots$) is plotted versus the flow-oscillation amplitude $\delta\beta$.

An analysis of the results shown in figure 8 indicates that the period doubling occurs as a result of a resonance between the drop tumbling motion and the vorticity oscillations. Namely, if the drop is relatively long and approximately aligned with the straining axis of the external flow when the vorticity parameter $\beta(t)$ reaches a minimum, the drop rotation may be significantly slowed down or even arrested (as in the long-drop stationary state discussed in §3). Such a temporary arrest of drop rotation corresponds to the shoulders in the plots of the angular evolution depicted in figure 8. On the other hand, if the drop angle exceeds $\phi = \pi/4$ when the vorticity goes through a minimum, the arrest of drop rotation does not occur. As seen in figure 8($b$) the interplay of drop tumbling with oscillations of the external forcing produces the period-doubling bifurcation that leads to alternating accelerated and retarded drop-rotation cycles.

The bifurcation diagrams shown in figures 9($a$) and 9($b$) illustrate the sensitivity of the period-doubling cascade to small variations of the system parameters. The two

---

† The only significant deviation from the quasi-static evolution for $T/t_\sigma \gg 1$ occurs right after the drop jumps from the long to the compact shape when $\beta$ increases above the upper critical value $\beta_2$. Namely, before the drop settles down to the compact stationary shape it undergoes a tumbling motion with the amplitude of length variation decaying on the time scale (3.2).
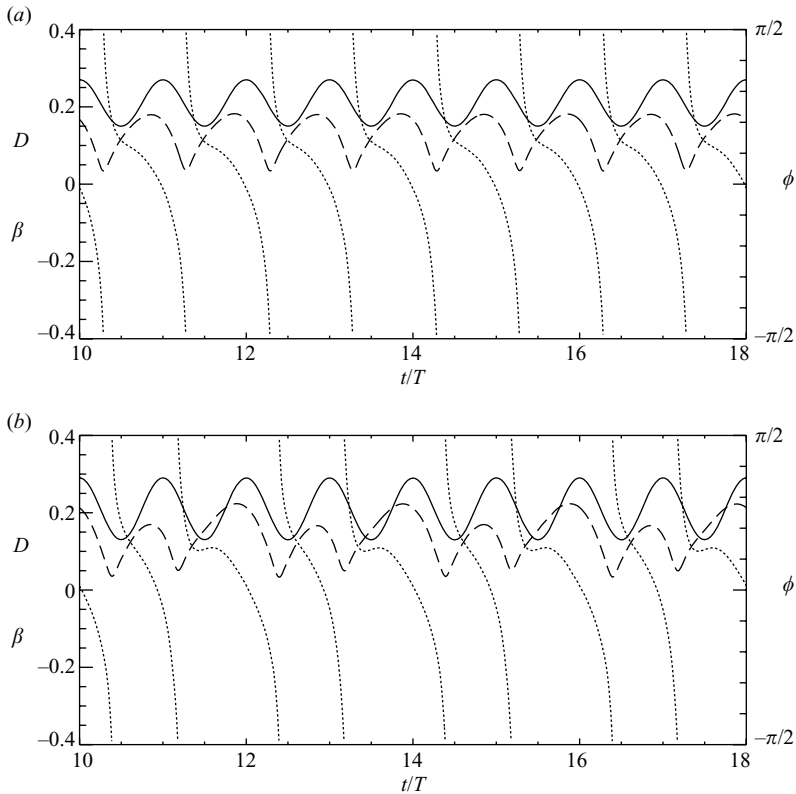
FIGURE 8. Period doubling in the dynamics of a viscous drop in two-dimensional linear flow with harmonic variation of vorticity. Vorticity parameter $\beta$ (solid lines), drop deformation $D$ (dashed), and drop angle $\phi$ (dotted) are shown versus time $t$ normalized by the oscillation period $T$. Viscosity ratio $\lambda = 275$, capillary number $Ca = 0.2$, period $T/t_\sigma = 1.14$, mean vorticity $\bar{\beta} = 0.21$, and vorticity oscillation amplitude (*a*) $\delta\beta = 0.06$ and (*b*) 0.08. (Results from small-deformation theory.)
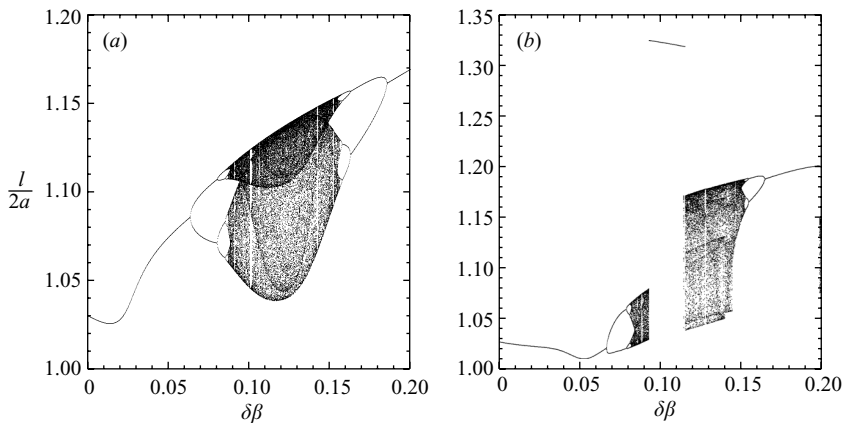


FIGURE 9. Bifurcation diagrams showing period-doubling cascades and transition to chaos for viscous drop in linear flow with harmonic vorticity variation with (*a*) mean $\bar{\beta} = 0.21$ and period $T/t_\sigma = 1.14$, and (*b*) mean $\bar{\beta} = 0.22$ and period $T/t_\sigma = 1.82$. For (*a*) the viscosity ratio and capillary number are the same as in figures 7 and 8. For (*b*) the viscosity ratio and capillary number are the same as in figure 11. (Results from small-deformation theory.)
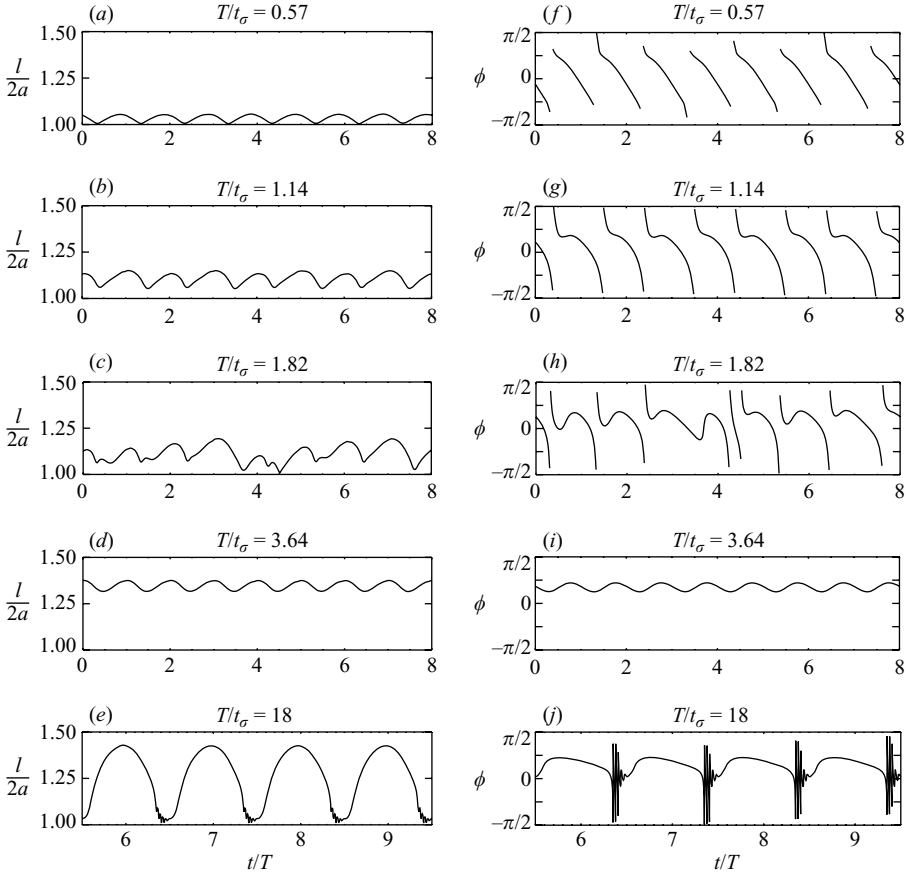
FIGURE 10. The same as figure 7, except that the results are from boundary-integral simulations and for slightly different values of oscillation period. The same $\bar{\beta}$ and $\delta\beta$ as in figure 7.

plots correspond to slightly different values of $\bar{\beta}$ and $T$; yet, the results are quite distinct. Not only has the position of the period-doubling bifurcations and the range of variation of the drop length changed, but also the chaotic domain in figure 9(*b*) disappears in the region $0.95 \lesssim \delta\beta \lesssim 0.115$.

In our numerical calculations depicted in figures 7–9 we have used the full set of the small-deformation equations (3.13), but we find that the simplified asymptotic equations (3.15) yield similar results. In particular, the simplified equations reproduce the cascade of the period-doubling bifurcations and the chaotic-evolution domain. (However, any further simplification of the evolution equations is not possible: if any of the terms in equations (3.15) is removed the solutions qualitatively change and the chaotic domain disappears.) We find that chaotic drop dynamics occurs only for highly viscous drops with $\lambda \gtrsim 200$.

### 4.2. *Boundary-integral results*

Figure 10 shows examples of our simulation results for the periodic and chaotic drop evolution. The flow parameters are similar to those used in our small-deformation calculations described in §4.1. As with the small-deformation calculations, for short periods of the external forcing $T$ the drop oscillates around the compact stationary shape, for moderate periods the system undergoes a transition to chaotic
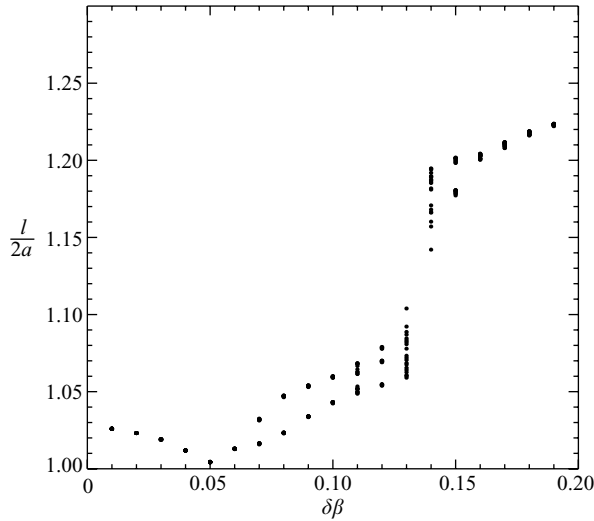
FIGURE 11. Bifurcation diagram for viscous drop in linear flow with harmonic vorticity variation with $\bar{\beta} = 0.22$, $T/t_\sigma = 1.82$, $\lambda = 275$, and $Ca = 0.2$. (Results from boundary-integral simulations.)

evolution, and for long periods the drop motion approaches the quasi-static behaviour. Consistent with the small-deformation results, the chaotic drop dynamics revealed by the boundary-integral simulations is associated with a cascade of period-doubling bifurcations. A bifurcation diagram illustrating this behaviour is presented in figure 11 for the system parameters corresponding to the small-deformation results depicted in figure 9(*b*).

A comparison of the results shown in figures 9(*b*) and 11 indicate that the domain of chaotic dynamics in the direct boundary-integral simulations somewhat differs from the corresponding domain obtained from the small-deformation theory. In the regions $0 \lesssim \delta\beta \lesssim 0.07$ and $0.15 \lesssim \delta\beta \lesssim 0.2$ the initial period-doubling bifurcations occur at approximately the same positions. However, the period-doubling cascade is shifted, and and a stable periodic solution found in the small-deformation theory for $0.092 \leqslant \delta\beta \leqslant 0.11$ does not appear in our boundary-integral simulations.

We have tested the convergence of our boundary-integral simulations, and we believe that the differences in the drop behaviour obtained using the two different methods stems primarily from the approximations involved in the small-deformation theory. We note, however, that drop evolution in the period doubling and chaotic regimes is very sensitive to small perturbations (as illustrated in figure 9). Hence, some differences in the bifurcation diagrams obtained from the two methods is expected.

## 5. Drop statistics in a linear flow with stochastic vorticity

In some systems, e.g. emulsion flows through a packed bed of fibres (Mosler & Shaqfeh 1997) or turbulent emulsion flows with drops that are much smaller than the Kolmogorov scale (Cristini *et al.* 2003*a*), a viscous drop undergoes deformation in a random external creeping flow. To gain some understanding of the role that drop bistability may play in such systems we consider the drop behaviour in a flow with stochastic vorticity.
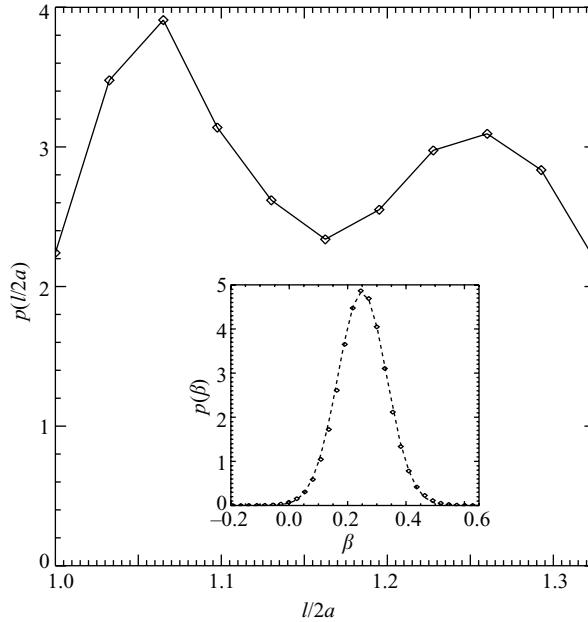
FIGURE 12. Length probability distribution for viscous drop with $\lambda = 200$ and $Ca = 0.2$, in linear flow with stochastic vorticity. Mean value of the vorticity parameter $\langle \beta \rangle = 0.25$, variance $\delta\beta = 0.13$, and correlation time $\tau^{corr}/t_\sigma = 0.24$. Inset shows vorticity probability distribution. (Results from boundary-integral simulations.)

We assume that the time variation of the vorticity parameter $\beta$ is described by a stationary Markovian Gaussian process (i.e. the Ornstein–Uhlenbeck process) with the mean $\langle \beta \rangle$, variance $\delta\beta$, and correlation time $\tau^{corr}$. A standard numerical scheme (Fox *et al.* 1988) for generating such a time-correlated Gaussian process is applied to model the time variation of $\beta$ along a drop trajectory. The results shown in figures 12–14 were obtained using a single long simulation run for each set of system parameters. Owing to the ergodicity of the process, the drop statistics along a single trajectory is equivalent to the stationary ensemble distribution.

An example of drop behaviour in a stochastic flow with a Gaussian variation of the vorticity is presented in figure 12. The mean value of the vorticity is $\langle \beta \rangle = 0.25$ and the variance is $\delta\beta = 0.13$. The correlation time of the vorticity distribution $\tau^{corr}/t_\sigma = 0.24$ is several times shorter than the drop-relaxation time. The figure depicts the probability distribution of the drop-length, obtained using the boundary-integral simulations. The capillary number is $Ca = 0.2$, and the drop viscosity is $\lambda = 200$.

The results indicate that the drop-length distribution is bimodal for the above parameter values. This behaviour is expected since the vorticity undergoes random variation in the domain that includes both the lower and upper critical values $\beta_1$, and $\beta_2$ of the vorticity parameter $\beta$. Since drop response to a flow with slow variation of vorticity is hysteretic, a drop in the random flow tends to stay in the neighbourhood of the compact and the elongated stationary states.

We note that the peak of the length probability distribution at $l \approx 1.25$ is shifted towards the shorter drop lengths compared to the length of a drop in the elongated stationary shape. This is because $Ca = 0.2$ is close to the critical capillary number for drop breakup. Thus, due to the slow time scale in the drop dynamics near the critical capillary number (see Blawzdziewicz *et al.* 2002, and the discussion in the Appendix),
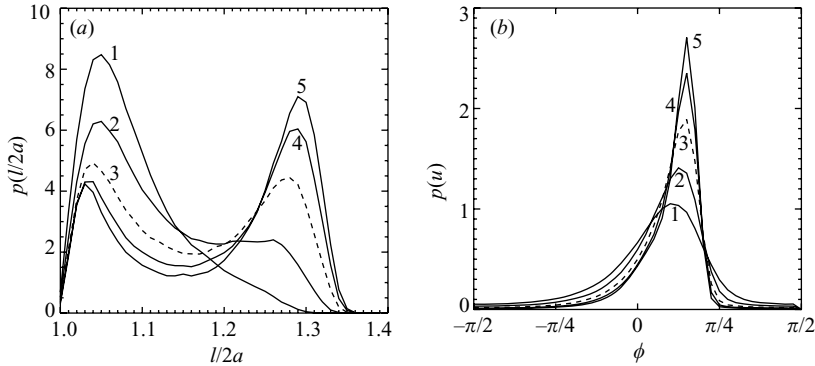
FIGURE 13. (*a*) Length and (*b*) angle probability distributions for viscous drop with $\lambda = 200$ and $Ca = 0.2$, in linear flows with stochastic vorticity. Mean and variance of the vorticity parameter are the same as in figure 12; the correlation times are $\tau^{corr}/t_\sigma = 0.025, 0.1, 0.2, 0.3, 0.4$ for lines marked 1–5, respectively. (Results from small-deformation theory.)
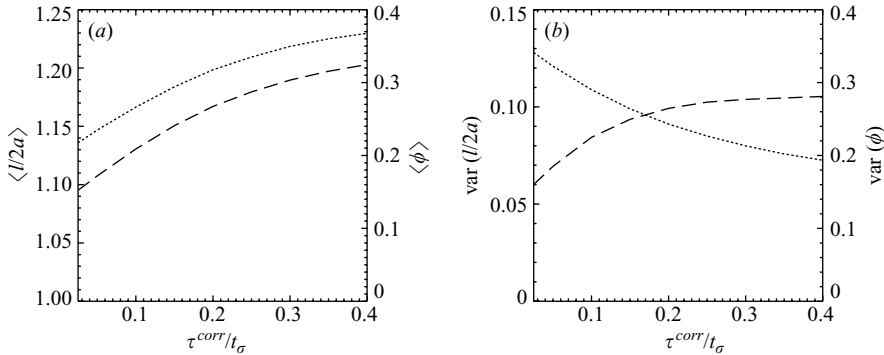


FIGURE 14. (*a*) Mean and (*b*) variance of drop length (dashed line) and angle (dotted) versus correlation time $\tau^{corr}$ normalized by the drop-deformation time, for $\lambda = 200$, $Ca = 0.2$, $\langle\beta\rangle = 0.25$, and $\delta\beta = 0.13$.

the drop does not have sufficient time to extend fully before the vorticity significantly changes.

Figure 13 shows the probability density for the drop length $l$ and drop angle $\phi$ for different values of the flow correlation time $\tau^{corr}$. (Other system parameters are the same as in figure 12.) The calculations were performed using the small-deformation equations (3.13). The results indicate that at short flow correlation times the drop-length probability distribution is peaked around small values corresponding to the short-drop stationary solution and has a moderate-height peak at $\phi \approx \pi/4$. As the flow correlation time $\tau^{corr}$ increases, the length probability distribution becomes bimodal: one of its peaks corresponds to compact and the other to elongated drops. A corresponding change occurs in the angle distribution, i.e. its peak becomes more pronounced, and shifts towards the straining axis $\phi = \pi/4$.

The shift of the typical drop length and orientation from the compact to elongated state when the flow correlation time is increased resembles the analogous shift for a system with harmonic vorticity oscillations (see figures 7*b, g* and 7*d, i*). This behaviour is further illustrated in figure 14, which shows the average values and the variance of $l$ and $\phi$ versus the correlation time $\tau^{corr}$.

## 6. Conclusions

We have presented results of numerical and theoretical investigations of the dynamics of highly viscous drops in two-dimensional linear creeping flows with time-dependent vorticity. In our earlier publication (Błtawzdziewicz *et al.* 2003) we predicted that in stationary flows such drops exhibit bistable behaviour: there is a range of system parameters where the drop may assume either an elongated shape approximately aligned with the straining axis of the external flow or a nearly spherical shape approximately aligned in the flow direction. Here the consequences of this behaviour for the system dynamics are analysed, and the physical mechanism that leads to drop bistability is elucidated.

A direct consequence of the existence of two stationary states is hysteretic drop response to a flow with slowly varying vorticity. We have explained that the rapid transition from an elongated non-rotating drop shape to the nearly spherical compact shape occurs when the vorticity becomes strong enough to overcome the effect of the straining flow component that aligns the drop with the straining axis. This transition is thus analogous to a similar instability that occurs for an elongated rigid particle which starts to tumble when the vorticity grows above a critical value (Jeffery 1922). A viscous drop also begins to tumble at a critical vorticity magnitude $\beta_2$. However, when the drop becomes misaligned with the extensional axis, it relaxes under the action of capillary forces towards a nearly spherical rotationally stabilized stationary shape.

If, in turn, the vorticity is slowly decreased, the drop returns to the elongated shape only after the vorticity magnitude reaches a lower critical value $\beta_1 < \beta_2$. This hysteretic drop response occurs in the high-viscosity regime because the rotational stabilizing mechanism is more efficient at high drop viscosities. A highly viscous drop deforms less within each drop revolution, so the compact shape remains stable even for relatively small vorticity magnitudes.

The existence of two stationary states affects drop dynamics not only in the quasi-static regime but also at finite frequencies of the external forcing. At small amplitudes of harmonic vorticity variation the drop simply oscillates (with the same frequency as the external forcing) about one of the stationary states. However, if the vorticity-variation range includes both critical values $\beta_1$ and $\beta_2$ the dynamics of the system is much richer. We find that with an increasing magnitude of the vorticity oscillations the system undergoes a cascade of period-doubling bifurcations resulting in chaotic drop dynamics. The period doubling stems from the resonance between the periodicity of the external forcing and the tumbling motion of the drop when it jumps from a (partially) elongated shape towards the compact rotationally stabilized state.

Chaos in our system emerges despite linearity of Stokes equations – the system dynamics is nonlinear because of the coupling of the flow to the evolving fluid interface. A detailed analysis of small-deformation equations describing drop dynamics reveals that, in addition to chaos associated with the period-doubling mechanism, there also exists in our system a different kind of chaotic evolution that results from manifold tangling (Guckenheimer & Holmes 1983*b*). Our analysis of different types of chaos will be presented in a separate publication.

To our knowledge, chaotic drop dynamics in Stokes-flow regime has never been observed before. We note, however, that in a recent independent study Kas-Danouche, Papageorgiou & Siegel (2007) have reported chaotic dynamics in co-annular Stokes flow with insoluble surfactant adsorbed on the fluid interface. Chaos in their system also appears via a period-doubling cascade.

Understanding of drop bistability and the associated dynamical phenomena is relevant for many practical problems. For example, interpretation of rheological response of emulsions of highly viscous drops to time-varying flows requires proper insight into drop dynamics. Our results may also be useful in designing new methods for manipulating emulsion microstructure in material processing and controlling drop behaviour in microfluidic flows. Drop bistability could, for instance be used to construct microfluidic switches, and chaotic drop dynamics may be relevant for microfluidic mixing.

The stabilizing and destabilizing mechanisms described in our paper apply not only to viscous drops but also to other deformable particles. Therefore, results of our study have a broader significance.

In particular, our analysis suggests that macromolecules with high degree of internal dissipation may undergo a transition between a nearly spherical and moderately elongated states (in addition to the standard coil-stretch transition predicted by de Gennes 1974). In fact, the dynamics of macromolecules can be modelled using equations analogous to (3.15), supplemented with terms representing random thermal forces. As shown in our preliminary study (Bławzdziewicz 2006), such a simplified description correctly captures the most important features of power spectra of DNA molecules evolving in linear flows with non-zero rotational component (cf. the review article by Shaqfeh 2005 on the dynamics of macromolecules in linear flows). Our analysis also explains the stabilizing effect of the rotational component of the flow on the compact molecule conformation.

There are also close analogies between drop and vesicle motion. The main difference between these two systems is that vesicles satisfy a constant-area constraint whereas the drop area can vary. This constraint gives rise to periodic vesicle motion (such as tank treading and tumbling) even in stationary flows (Misbah 2006; Vlahovska & Gracia 2007). It would be interesting to determine if a coupling of vesicle oscillations to a harmonic variation of the external flow can lead to chaotic dynamics.

It would also be of significant interest to experimentally explore the bistable and chaotic drop dynamics (as well as related phenomena for other deformable particles). In such experiments a four-roll mill could be used to produce a linear flow with a controlled magnitude of vorticity. The experiments could also be performed using recently developed microfluidic analogues of a four-roll mill device (Hudson *et al.* 2007; Lee *et al.* 2007).

## Appendix. Highly viscous drops in near-critical regime: Physical sources of numerical inaccuracies

Simulations of the hysteretic evolution of high-viscosity drops are numerically demanding because of two inherent physical features of the system. First, drop relaxation towards the stationary state is very slow; and second, in the relevant parameter range, the drop length is very sensitive to small perturbations. Both these features result from a critical behaviour near the bifurcation points that characterize the system dynamics. The relaxation time is in addition significantly increased owing to high drop viscosity.

### Critical slowing down

As discussed by Bławzdziewicz *et al.* (2002) (also see Bławzdziewicz *et al.* 1998; Navot 1999), near a bifurcation point $Ca = Ca_{crit}$ at which a given branch of stationary drop shapes loses its stability, the stabilizing and destabilizing stresses balance each

other. This causes a slow evolution of the drop shape on the time scale $t_{crit} \sim \delta Ca^{-1/2}$, where

$$\delta Ca = |Ca - Ca_{crit}| \tag{A 1}$$

is the distance from the bifurcation point. For our present system, the critical point $Ca = Ca_{crit}$ corresponds either to a transition between the elongated and compact stationary shapes at a given value of the vorticity $\beta$, or to the instability that results in drop breakup. A slow evolution also occurs near the cusp bifurcation leading to the emergence of the two coexisting branches of stationary states.

For highly viscous drops the evolution outside the near-critical regime occurs on the time scale (3.1). Taking into account the critical slowing down we thus have

$$t_{crit} = \delta Ca^{-1/2} \lambda \dot{\gamma}^{-1}. \tag{A 2}$$

The two large factors $\delta Ca^{-1/2}$ and $\lambda$ in equation (A 2) imply that very long simulation runs are required to obtain quasi-static drop behaviour in the region near the bifurcation points. Moreover, while the evolution of the slowest mode occurs on the slow time scale (A 2), the size of the numerical time step is limited by the stability requirements associated with the much faster relaxation of the short-wave perturbations of the drop shape and with the rotational relaxation on a short time scale $\dot{\gamma}^{-1}$. Therefore, a large number of time steps is required to obtain quasi-static results.

*Critical susceptibility*

As indicated by Błamdziewicz *et al.* (2002), the stationary drop length near a bifurcation point exhibits the critical behaviour

$$l = l_{crit} - \alpha \, \delta Ca^{1/2}, \tag{A 3}$$

where $l_{crit}$ is the critical length and $\alpha$ is a proportionality constant. The critical behaviour (A 3) implies that the stationary drop length $l$ is very sensitive to small perturbations of the system. This is because even a small shift of the critical point can result in a significant change of $l$. Such a shift may occur as a result of discretization errors or approximations used in a small-deformation description of drop dynamics.

The sensitivity of the stationary shape to small perturbations implies that a much larger number of mesh nodes $N$ is needed to achieve an assumed numerical accuracy near a critical point than outside a near-critical regime. In particular, the approximately 1 % differences between the drop length $l$ for the upwards and downwards ramps of vorticity parameter $\beta$, seen in figure 4 for $Ca = 0.2$, stem from numerical inaccuracies magnified by the large susceptibility to small perturbations near the critical point for drop breakup. The most challenging simulation run for viscosity ratio $\lambda = 200$ and $Ca = 0.2$ required $N \approx 10^3$ mesh nodes on the drop surface. Moreover, a very long ramping period ($T = 8 \times 10^4 \dot{\gamma}$) was needed to ensure the quasi-static behaviour of the drop shape. The whole simulation run thus required several weeks of CPU time on a fast Linux workstation.

In the above discussion, the distance of the system from the critical point is characterized in terms of the capillary parameter (A 1) at a given value of $\beta$. However, analogous results would also be obtained if the distance from the critical point is measured in terms of the vorticity parameter $\delta\beta = |\beta - \beta_{crit}|$ at a fixed value of the capillary number. In particular, the critical behaviour $l - l_{crit} \sim \beta^{1/2}$ is seen in figures 2, 4, and 6 for $\beta$ near a critical value $\beta_1$ or $\beta_2$. In general, the square-root behaviour of the relaxation time scale and of the amplitude of the critical mode in the stationary solution is characteristic for autonomous dynamical systems near a turning-point bifurcation (Drazin 1992).

## REFERENCES

BARTHÈS-BIESEL, D. & ACRIVOS, A. 1973 Deformation and burst of a liquid droplet freely suspended in a linear shear field. *J. Fluid Mech.* **61**, 1–21.

BENTLEY, B. J. & LEAL, L. G. 1986 An experimental investigation of drop deformation and breakup in steady, two-dimensional linear flows. *J. Fluid Mech.* **167**, 241–283.

BIGIO, D. I., MARKS, C. R. & CALABRESE, R. V. 1998 Predicting drop breakup in complex flows from model flow experiments. *Intl. Polymer Process.* **13**, 192–198.

BŁAWZDZIEWICZ, J. 2006 Boundary integral methods for Stokes flows. In *Computational Methods for Multiphase Flow* (ed. A. Prosperetti & G. Tryggvason). Cambridge University Press.

BŁAWZDZIEWICZ, J., CRISTINI, V. & LOEWENBERG, M. 1997 Analysis of drop breakup in creeping flows. *Bull. Am. Phys. Soc.* **42**, 2125.

BŁAWZDZIEWICZ, J., CRISTINI, V. & LOEWENBERG, M. 1998 Critical conditions for drop breakup in linear flows. *Bull. Am. Phys. Soc.* **43**, 2066.

BŁAWZDZIEWICZ, J., CRISTINI, V. & LOEWENBERG, M. 2002 Critical behavior of drops in linear flows. I. Phenomenological theory for drop dynamics near critical stationary states. *Phys. Fluids* **14**, 2709–2718.

BŁAWZDZIEWICZ, J., CRISTINI, V. & LOEWENBERG, M. 2003 Multiple stationary states for deformable drops in linear Stokes flows. *Phys. Fluids* **15**, L37–40.

BORWANKAR, R. P. & CASE, S. E. 1997 Rheology of emulsions, foams and gels. *Curr. Opin. Colloid Interface Sci.* **2**, 584–589.

CRISTINI, V., BŁAWZDZIEWICZ, J. & LOEWENBERG, M. 1998 Drop breakup in three-dimensional viscous flows. *Phys. Fluids.* **10**, 1781–1784.

CRISTINI, V., BŁAWZDZIEWICZ, J. & LOEWENBERG, M. 2001 An adaptive mesh algorithm for evolving surfaces: Simulations of drop breakup and coalescence. *J. Comput. Phys.* **168**, 445–463.

CRISTINI, V., BŁAWZDZIEWICZ, J., LOEWENBERG, M. & COLLINS, L. R. 2003a Breakup in stochastic Stokes flows: Sub-Kolmogorov drops in isotropic turbulence. *J. Fluid Mech.* **492**, 231–250.

CRISTINI, V., GUIDO, S., ALFANI, A., BŁAWZDZIEWICZ, J. & LOEWENBERG, M. 2003b Drop breakup and fragment size distribution in shear flow. *J. Rheol.* **47**, 1283–1298.

CRISTINI, V. & TAN Y.-C. 2004 Theory and numerical simulation of droplet dynamics in complex flows – A review. *Lab Chip* **4**, 257–264.

DRAZIN, P. G. 1992 *Nonlinear Systems*. Cambridge University Press.

FOX, R. F., GATLAND, I. R., ROY, R. & VEMURI, R. 1988 Fast, accurate algorithm for numerical simulation of exponentially correlated colored noise. *Phys. Rev.* A **38**, 5938.

GRIGORIEV, R. O., SCHATZ, M. F. & SHARMA, V. 2006 *Lab Chip* **6**, 1369–1372.

GUCKENHEIMER, J. & HOLMES, P. 1983 *Nonlinear Oscillations, Dynamical Systems, and Bifurcations of Vector Fields*. Springer.

DE GUENNES, P. G. 1974 Coil-stretch transition of dilute flexible polymers under ultrahigh velocity gradients. *J. Chem. Phys.* **60**, 5030–5042.

GUIDO, S., GROSSO, M. & MAFFETTONE, P. L. 2004 Newtonian drop in a Newtonian matrix subjected to large amplitude oscillatory shear flows. *Rheol. Acta* **43**, 575–583.

GUIDO, S., MINALE, M. & MAFFETTONE, P. L. 2000 Drop shape dynamics under shear-flow reversal. *J. Rheol.* **44**, 1385–1399.

HUDSON, S. D., PHELAN, F. R., HANDLER, M. D., CABRAL, J. T., MIGLER, K. B. & AMIS, E. J. 2007 Microfluidic analog of the four-roll mill. *Appl. Phys. Lett.* **85**, 335–337.

JEFFERY, G. 1922 The motion of ellipsoidal particles immersed in a viscous fluid. *Proc. Roy. Soc.* A **102**, 161–179.

KAS-DANOUCHE, S., PAPAGEORGIOU, D. T. & SIEGEL, M. 2007 Nonlinear dynamics of core-annular film flows in the presence of surfactant. *J. Fluid Mech.* (submitted).

KENNEDY, M. R., POZRIKIDIS, C. & SKALAK, R. 1994 Motion and deformation of liquid drops and the rheology of dilute emulsions in simple shear flow. *Comput. Fluids* **23**, 251–278.

LEE, J. S., DYLLA-SPEARS, R., TECLEMARIAM, N. P. & MULLER, S. J. 2007 Microfluidic four-roll mill for all flow types. *Appl. Phys. Lett.* **90**, 074103.

LISTER, J. R. & STONE, H. A. 1998 Capillary breakup of a viscous thread surrounded by another viscous fluid. *Phys. Fluids* **10**, 2758–2764.

MADER, M.-A., VITKOVA, V., ABKARIAN, M., VIALLAT, A. & PODGORSKI, T. 2006 Dynamics of viscous vesicles in shear flow. *Eur. Phys. J.* E **19**, 389–397.

MASON, T. G. 1999 New fundamental concepts in emulsion rheology. *Curr. Opin. Colloid Interface Sci.* **4**, 231–238.

MISBAH, C. 2006 Vacillating breathing and tumbling of vesicles under shear flow. *Phys. Rev. Lett.* **96**, 028104.

MOSLER, A. B. & SHAQFEH, E. S. G. 1997 Drop breakup in the flow through fixed beds via stochastic simulation in model Gaussian fields. *Phys. Fluids* **9**, 3209–3226.

NAVOT, Y. 1999 Critical behavior of drop breakup in axisymmetric viscous flow. *Phys. Fluids* **11**, 990–996.

POZRIKIDIS, C. 1992 *Boundary Integral and Singularity Methods for Linearized Viscous Flow*. Cambridge University Press.

RALLISON, J. M. 1980 Note on the time-dependent deformation of a viscous drop which is almost spherical. *J. Fluid Mech.* **98**, 625–633.

RALLISON, J. M. & ACRIVOS, A. 1978 Numerical study of deformation and burst of a viscous drop in an extensional flow. *J. Fluid Mech.* **89**, 191–200.

RENARDY, Y. 2006 Numerical simulation of a drop undergoing large amplitude oscillatory shear. *Rheol. Acta* **45**, 223–227.

SHAQFEH, E. S. G. 2005 The dynamics of single-molecule DNA in flow. *J. Non-Newtonian Fluid Mech.* **130**, 1–28.

SONG, H., CHEN, D. L. & ISMAGILOV, R. F. 2006 *Angew. Chem. Int. Ed.* **45**, 7336–7356.

TAN, Y. C., FISHER, J. S., LEE, A. I., CRISTINI, V. & LEE, A. P. 2004 Design of microfluidic channel geometries for the control of droplet volume, chemical concentration, and sorting. *Lab Chip* **6**, 954–957.

TAYLOR, G. I. 1934 The formation of emulsions in definable fields of flow. *Proc. R. Soc. Lond.* A **146**, 501–523.

TORZA, S., COX, R. G. & MASON, S. G. 1972 Particle motions in sheared suspensions XXVII. Transient and steady deformation and burst of liquid drops. *J. Colloid Interface Sci.* **38**, 395–411.

TUCKER III, C. L. & MOLDENAERS, P. 2002 Microstructural evolution in polymer blends. *Ann. Rev. Fluid Mech.* **34**, 177–210.

VLAHOVSKA, P. M. 2003 Dynamics of surfactant-covered drops and the non-Newtonian rheology of emulsions. PhD thesis, Yale University.

VLAHOVSKA, P., BŁAWZDZIEWICZ, J. & LOEWENBERG, M. 2005 Deformation of a surfactant-covered drop in a linear flow. *Phys. Fluids* **17**, 103103.

VLAHOVSKA, P. M., BŁAWZDZIEWICZ, J. & LOEWENBERG, M. 2008 Small-deformation theory for a surfactant-covered drop in linear flows. *J. Fluid Mech.* (submitted).

VLAHOVSKA, P. M. & GRACIA, R. S. 2007 Dynamics of a viscous vesicle in linear flows. *Phys. Rev.* E **75**, 016313.

WHITESIDES, G. M. & STROOCK, A. D. 2001 Flexible methods for microfluidics. *Phys. Today* **54**, 42–48.

WINDHAB, E. J., DRESSLER, M., FEIGL, K., FISCHER, P. & MEGIAS-ALGUACIL, D. 2005 Emulsion processing: From single-drop deformation to design of complex processes and products. *Chem. Engng Sci.* **60**, 2101–2113.

ZINCHENKO, A. Z., ROTHER, M. A. & DAVIS, R. H. 1999 Cusping, capture, and breakup of interacting drops by a curvatureless boundary-integral algorithm. *J. Fluid Mech.* **391**, 249–292.